Stellar Rotation in Young Clusters.
I. Evolution of Projected Rotational Velocity Distributions

W. Huang and D. R. Gies[1]

Center for High Angular Resolution Astronomy
Department of Physics and Astronomy
Georgia State University, P. O. Box 4106, Atlanta, GA 30302-4106;
huang@chara.gsu.edu, gies@chara.gsu.edu

ABSTRACT

Open clusters offer us the means to study stellar properties in samples with well-defined ages and initial chemical composition. Here we present a survey of projected rotational velocities for a large sample of mainly B-type stars in young clusters to study the time evolution of the rotational properties of massive stars. The survey is based upon moderate resolution spectra made with the WIYN 3.5 m and CTIO 4 m telescopes and Hydra multi-object spectrographs, and the target stars are members of 19 young open clusters with an age range of approximately 6 to 73 Myr. We made fits of the observed lines He I $\lambda\lambda 4026, 4387, 4471$ and Mg II $\lambda 4481$ using model theoretical profiles to find projected rotational velocities for a total of 496 OB stars. We find that there are fewer slow rotators among the cluster B-type stars relative to nearby B stars in the field. We present evidence consistent with the idea that the more massive B stars ($M > 9 M_\odot$) spin down during their main sequence phase. However, we also find that the rotational velocity distribution appears to show an increase in the numbers of rapid rotators among clusters with ages of 10 Myr and higher. These rapid rotators appear to be distributed between the zero age and terminal age main sequence locations in the Hertzsprung-Russell diagram, and thus only a minority of them can be explained as the result of a spin up at the terminal age main sequence due to core contraction. We suggest instead that some of these rapid rotators may have been spun up through mass transfer in close binary systems.

---

[1]Visiting Astronomer, Kitt Peak National Observatory and Cerro Tololo Interamerican Observatory, National Optical Astronomy Observatory, operated by the Association of Universities for Research in Astronomy, Inc., under contract with the National Science Foundation.

Subject headings: line: profiles — stars: rotation — stars: early-type — open clusters and associations: individual (Berkeley 86, IC 1805, IC 2395, IC 2944, NGC 457, NGC 869, NGC 884, NGC 1502, NGC 2244, NGC 2362, NGC 2384, NGC 2422, NGC 2467, NGC 3293, NGC 4755, NGC 6193, NGC 7160, Trumpler 14, Trumpler 16)

1. Introduction

Unlike low mass stars that can lose their angular momentum early in their main sequence phase, massive OB stars are usually born with a large initial angular momentum that can last throughout their relatively short, core hydrogen-burning phase. The spin evolution of a single, non-magnetic, massive star is driven by angular momentum loss in the stellar wind, a net increase in the moment of inertia, and an increase in stellar radius. Theoretical models of these processes were recently developed independently by Heger & Langer (2000) and Meynet & Maeder (2000). These models predict the changes in the stellar interior, the equatorial rotational velocity, and photospherical chemical abundances that occur along the evolutionary tracks. One of the predictions of these models is that massive stars spin down during core H-burning at a rate that is larger for more massive stars and for those with higher initial rotational speeds. These models predict that a spin-up episode can occur very close to the terminal age main sequence (TAMS) when the core contracts prior to H-shell burning. In some situations this increase may lead to near critical rotational velocities and induce enhanced equatorial mass outflows such as are observed in rapidly rotating Be stars (Maeder, Grebel, & Mermilliod 1999; Zorec 2004). Fabregat & Torrejón (2000) found that the incidence of Be stars tends to peak in open clusters with ages between 13 and 25 Myr, approximately when early B-type stars are close to the TAMS. A similar conclusion was also found by McSwain & Gies (2005) based upon a study of the frequency of Be stars in some 48 southern sky clusters. However, the positions of the Be stars in the Hertzsprung-Russell diagram (HRD) cover the entire range between the zero-age main sequence (ZAMS) and the TAMS (Mermilliod 1982; Zorec 2004; McSwain & Gies 2005) so it is doubtful that many Be stars are actually TAMS objects.

Another possible process causing spin-up in massive stars is mass transfer in close binary systems. There are many examples of rapid rotation of the mass gainer in close binaries (van den Heuvel 1970; Etzel & Olson 1993; Šimon 1999; Barai et al. 2004). Even moderate mass transfer can cause a significant spin up of the mass gainer star (Langer et al. 2004). One extreme example of this spin up process is found in the classical Be star, ϕ Persei, which was probably spun up by an earlier stage of mass transfer to attain the observed projected

rotational velocity of $V \sin i = 450$ km s^{-1} (about 97% of the critical velocity; Gies et al. 1998).

Young star clusters provide us with examples of stellar populations that probably started with the same chemical composition and are now observed with various well-defined ages. Spectroscopic analysis of the stars in young clusters offers us the means to examine these various processes affecting rotation. Here we present an investigation of the stellar rotation properties of the brighter stars in 19 open clusters with an age range between 6 and 73 Myr. In §2 we describe the observing runs and data reduction procedures, and in §3 we outline the details of the line synthesis method we used to determine the stellar projected rotational velocity $V \sin i$. We report in §4 on the statistical results based on the measured $V \sin i$ and some implications of these results for evolutionary models.

2. Observations

We obtained moderate dispersion, blue spectra of B-type stars in 19 Galactic clusters. We used the WEBDA open cluster database[2] (Mermilliod & Paunzen 2003) to select clusters for this study based on the following criteria: (1) age $<$ 75 Myr, (2) distance modulus $m-M < 15$, (3) angular diameter $10 - 60$ arcmin, and (4) more than 20 main sequence and/or giant star members with MK classifications of B9 or earlier. The names of these clusters are listed below (Table 4). The spectra of the northern sky clusters were obtained with the WIYN 3.5 m telescope at Kitt Peak National Observatory while the southern clusters were observed with the Cerro Tololo Interamerican Observatory 4 m telescope. Both telescopes are equipped with Hydra multiple-object spectrographs (Barden & Armandroff 1995) that use micropositioners and fiber optics to obtain spectra of many targets simultaneously. Our main goal was to record the absorption line profiles of He I $\lambda\lambda 4026, 4387, 4471$, Mg II $\lambda 4481$, and Hγ $\lambda 4340$ that are relatively strong throughout the B-type spectral class. We generally observed each cluster field on at least two nights, so that we could make a preliminary identification of the radial velocity variable stars (candidate spectroscopic binaries) and double-lined binaries (whose line profiles may mimic those of rapid rotators at some orbital phases).

The details of the spectrograph set up for each run are summarized in Table 1. The Hydra spectra from the two runs are comparable but the WIYN spectra have better resolving power than those from CTIO. All the targets in a particular cluster were observed in a single fiber configuration using multiple exposures of 10 minutes (CTIO) or 20 minutes (WIYN)

---

[2]http://www.univie.ac.at/webda/

duration. Additional fibers were set on the blank sky to estimate the sky background. In addition to nightly bias and dark frames, we also obtained flat field spectra for every fiber configuration and telescope pointing. We typically obtained spectra of 30 – 80 stars in each observation, but we report here only on the brighter B-type stars that we identified in each field.

All the spectra and calibration frames were reduced using standard routines in IRAF[3]. The extraction and calibration of the individual spectra from the images was done using the *dohydra* package (Valdes 1992), in which flat fielding is accomplished by dividing the stellar spectrum by the flat field spectrum after extraction. The individual sub-exposures were extracted separately and then co-added to improve the S/N ratio. All the spectra were transformed to a uniform wavelength scale and rectified to a unit continuum, and most have a S/N = 50 – 400 pixel^{-1} (depending on the star's brightness). The focus of each spectrograph varied slightly across the spectrum, and we used width measurements of the unresolved comparison lines to estimate the FWHM of the resolution element (yielding the instrumental spectral line broadening) at the positions of the important spectral features. These are listed in the last three rows of Table 1.

3. Measuring Projected Rotational Velocities

Rotational broadening is the process that dominates the apparent shapes of photospheric absorption lines in unevolved B-type stars, and the derivation of a projected rotational velocity ($V \sin i$) from their shape is the first step to study stellar rotation. One simple way to characterize these broadened line profiles is by measuring a line width (such as FWHM). The $V \sin i$ value can be directly determined if the relation between the line width and $V \sin i$ is carefully calibrated (Slettebak et al. 1975; Howarth et al. 1997). This method has been developed and improved over many decades, and it has become the dominant method in this field because of its simplicity and efficiency for processing large amounts of spectral data. However, since this method is based only upon the line width to gauge the effects of rotation on the line profile, the accuracy of the results may suffer. Furthermore, in the case of fast stellar rotation line width measurements become less useful due to the reduction in wing strength caused by strong gravity darkening of the equatorial flux in the stellar atmosphere (Townsend, Owocki, & Howarth 2004).

---

[3]IRAF is distributed by the National Optical Astronomy Observatory, which is operated by the Association of Universities for Research in Astronomy, Inc., under cooperative agreement with the National Science Foundation.

One way to solve this problem and to obtain more reliable and accurate $V \sin i$ measurements is by fitting the entire observed line profile with a grid of the theoretical calculations (Howarth & Smith 2001; Mathys et al. 2002; Townsend et al. 2004). Because this method uses all the available line data, we can derive a secure value for $V \sin i$ and help establish other physical properties such as effective temperature, gravity, and chemical abundance. The key to the success of this method is to begin by constructing reliable theoretical line profiles. It is often assumed for the sake of simplicity that the local intensity profiles have a Gaussian or Lorentzian shape, and then flux profiles are calculated by integrating these shapes over the visible, limb-darkened stellar surface. However, in this paper we will mainly examine He I lines that have specific intensity profiles that are too complicated to be described by Gaussian or Lorentzian functions. Therefore, we decided to calculate realistic intensity profiles using the stellar atmosphere code TLUSTY and the radiative transfer code SYNSPEC (Hubeny & Lanz 1995).

For hotter stars ($T_{\rm eff} > 13000$ K), we choose to fit the He I lines with the synthesized profiles based on intensity profiles calculated by TLUSTY and SYNSPEC, while we modeled and fit the Mg II $\lambda 4481$ line for the cooler, late-type B stars. We first calculated a set of simple H-He LTE model atmospheres using TLUSTY, assuming solar abundances and a constant microturbulent velocity (2 km s^{-1}). We then constructed a grid of specific intensity profiles using SYNSPEC that was based on a three dimensional parameterization using μ, the cosine of the angle between the surface normal and line of sight, $T_{\rm eff}$, the local effective temperature, and $\log g$, the logarithm of the surface gravity. The effective temperature ranges from $T_{\rm eff} = 12000$ K to 34000 K in steps of $2000°$ for the He I lines (and from 8000 K to 20000 K for the Mg II line); the surface gravity spans the range from $\log g = 3.2$ to 4.2 in steps of 0.2 dex; and the orientation cosine ranges from $\mu = 0.1$ to 1.0 in steps of 0.1.

We then integrated the flux contributions over the visible hemisphere of the model star to obtain the synthesized line profiles. The synthesis procedure included: (1) dividing the stellar surface into a large number of facets with approximately equal area (10000 - 20000 facets); (2) finding $T_{\rm eff}$ and $\log g$ at the center of each facet, by considering the Roche geometry for a point-like (condensed) mass distribution and the consequent gravity darkening caused by stellar rotation (Collins & Harrington 1966); (3) calculating the specific intensity as a function of wavelength across the profile for each facet by interpolating within the grid of specific intensity profiles described above; (4) integrating the contribution from all visible facets, Doppler-shifted properly and weighted by the projected area; and (5) rectifying the final output to a unit continuum.

Note that these profiles are based upon simple model atmospheres that neglect line blanketing, so that our assigned effective temperatures may be somewhat hotter than the

actual values. However, the change in the width of the intensity profiles caused by the adoption of an elevated temperature has a negligible impact on our derived projected rotational velocities because the rotational broadening is so much larger than the thermal and pressure broadening. We checked the reliability of this approach by calculating synthetic model profile fits using both unblanketed and blanketed model atmospheres (from the Kurucz code ATLAS9 for Linux[4]) for a sample of three stars that cover the observed range in projected line broadening, and we found that the derived values of $V \sin i$ were identical within errors in each case. Thus, our use of simple LTE models is satisfactory for the purpose of determining $V \sin i$ from line profiles.

We compared our model He I and Mg II profiles directly with those in the observed spectra to estimate the appropriate temperature model that we parameterized by a spectral subtype index. Table 2 lists the physical parameters (effective temperature, mass, radius) for the model grid that were selected and/or interpolated to correspond approximately to a pseudo-spectral subtype according to the spectral subtype – temperature calibrations given by Hanson, Howarth, & Conti (1997) (for the hotter subtypes) and by Gray (1992) (for the cooler subtypes). The He I lines increase in strength to a maximum near subtype B2 and then begin to decline, but we can distinguish between the hot and cool portions of the He I curve by the appearance of Mg II, which declines monotonically with increasing temperature in the B-star range. We found the best fit profile from the grid for each available line, and we adopted the average spectral subtype index for models used in the rotational broadening analysis. We caution that these indices may not correspond to an actual MK subtype for a number of reasons: (1) we are assuming for fitting purposes that the stars are main sequence objects, but many are in fact evolved stars (i.e., giants); (2) the assumption of a He solar abundance will not be accurate for the He-peculiar B-stars; (3) there may be line blending problems for the spectroscopic binary targets; and (4) the theoretical line profiles are based on simple H-He LTE, unblanketed atmosphere models that may yield a slightly different spectral subtype – temperature relation than adopted elsewhere. For example, we compared a series of synthetic profiles of He I $\lambda 4471$ calculated from both unblanketed and line-blanketed main sequence models, and these show that a given line equivalent width is matched by an unblanketed model with a temperature that is $\approx 15\%$ higher than that for line-blanketed model atmospheres for B-stars with $T_{\mathrm{eff}} < 22000$ K (and about $\approx 4\%$ higher for stars hotter than this). Therefore, the spectral subtype index from Table 2 that is assigned to a target star may be of a slightly earlier type than would be determined by actual spectral classification. In the next paper in this series (Huang & Gies 2006), we will fit the Hγ and He I spectral lines using fully line blanketed atmospheres in order to derive

---

[4]http://www.hs.uni-hamburg.de/DE/Ins/Per/Reiners/package.htm

the temperature, gravity, and He abundance of each target.

We constructed rotational line profiles for each line and for each spectral subtype index over a grid of projected rotational velocities ($V \sin i = 0$, 50, 100, 150, 200, 250, 300, 350, and 400 km s^{-1}) with a fixed inclination angle of $i = 90°$ (corresponding to a line of sight in the equatorial plane of the star). Finally, all the synthesized profiles were convolved with proper instrumental broadening profiles (Table 1) before comparison with the observations. For each spectrum we first estimated the spectral subtype index, determined an approximate projected rotational velocity, and then made a final fit after applying small corrections for the radial velocity shift and continuum placement. We found solutions for $V \sin i$ that minimized the χ^2 difference between the observed and calculated profiles for the adopted spectral subtype, and then formed an average based on all the available lines. Examples of the fitting procedure are illustrated in Figure 1 for a fast rotator (*top panels*) and a slow rotator (*bottom panels*) in the cluster NGC 884 (χ Per).

The measurement errors varied among our sample stars, depending on their magnitudes, spectral subtypes, and observing set up. Measurements of the He I lines in spectra of stars of subtypes later than B7 are difficult because the lines are weaker and often blended with nearby metallic transitions. For the cooler B stars ($T_{\rm eff} \leq 13000$ K) we relied on fits of the Mg II $\lambda 4481$ spectral region (which included Ti II $\lambda 4468$, He I $\lambda 4471$, Fe II $\lambda 4473$, and Fe I $\lambda 4476$). A comparison of the derived $V \sin i$ values among a sub-sample of late B-type stars where the He I and Mg II lines have comparable strength shows that we obtain the same projected rotational velocity within errors from fits of both line species. The average inter-line error on $V \sin i$ is about 10% for the CTIO data and about 5% for the WIYN data. The systematic errors introduced by our choice of spectral subtype index are similar in size. The difference in the derived $V \sin i$ measurement is generally $< 5\%$ when we compare results obtained using two adjacent spectral subtypes (see Table 2) and in fact decreases to zero around the B2 stars where the strength of the He I lines reaches a maximum and becomes insensitive to temperature. The measured errors $\delta V \sin i$ for individual stars (Table 3, column 4) are estimated using the He I $\lambda 4471$ or Mg II $\lambda 4481$ line fit. We define $\delta V \sin i$ as the offset from the best fit $V \sin i$ that increases the mean square of the deviations from the fit rms^2 by $2.7 {\rm rms}^2_{\rm min}/N$ (90% confidence level), where N is the number of wavelength points within the fit region and ${\rm rms}^2_{\rm min}$ is the best fit minimum mean square of the deviations. Note that the resolution of our spectra (Table 1) limits our ability to measure $V \sin i$ accurately in very narrow-lined stars, so stars with $V \sin i < {\rm FWHM}/2$ probably have $V \sin i$ errors of approximately $\pm {\rm FWHM}/2$ (29 and 48 km s^{-1} for the WIYN and CTIO spectra, respectively).

We found $V \sin i$ measurements in the WEBDA database on open clusters (Mermilliod & Paunzen 2003) for 69 stars in common with our sample (Slettebak 1965, 1968, 1985;

Hill 1967; Balona 1975a; Dworetsky 1975; Wolff 1981; Arnal et al. 1988; Verschueren 1991; Penny 1996; Mathys et al. 2002). Some 90% of these published $V \sin i$ values were obtained by simple visual estimates or by measuring line widths, but Mathys et al. (2002) measured $V \sin i$ in 6 stellar spectra using line profile fitting and a simple convolution scheme for rotational broadening. Our $V \sin i$ values are generally in good agreement with these results (Fig. 2), which can be fit by a linear relation,

$$V \sin i \text{ [Published]} = (0.91 \pm 0.05) \ V \sin i \text{ [Ours]} + (26 \pm 8) \text{ km s}^{-1}. \tag{1}$$

A large scatter is not unexpected in such a comparison because of the heterogeneity of the $V \sin i$ data sources and measurement techniques. Our results are systematically larger than the published ones by about 9%, which is probably due to our treatment of gravity darkening effects for fast rotators that accounts for the weaker line wings. The larger $V \sin i$ measurements for the published results in the low $V \sin i$ regime probably reflect the lower resolving power and S/N of the observations used in earlier studies.

We offer some cautionary remarks before consideration of our results in the next section. The run of stellar parameters as a function of temperature or spectral subtype in Table 2 is probably reliable for slow rotators. However, for fast rotators the physical conditions on the stellar surface can be quite different from non-rotating models due to the rotational effects. For example, Meynet & Maeder (1997) point out that the polar temperature of a fast rotator may be much higher than its effective temperature as derived from either the integrated luminosity and surface area or from the integrated spectrum of its visible hemisphere. Our scheme relies on a temperature estimate from the average line properties formed over the visible hemisphere, and we then adopt this temperature as the polar temperature in the calculation of a sequence of rotating star profiles. This inconsistency will have only a minor affect on our derived $V \sin i$ values because the profile shapes are much more dependent on the Doppler shifts caused by rotation than on the adopted temperature of the local atmosphere.

A similar problem may arise because of our assumption of solar abundances. Many He-strong and He-weak stars are known to exist among the B-stars (Mathys 2004), and since our temperature estimation scheme is based on He I line strengths, some of our derived spectral subtype estimates may be incorrect. However, even in these cases the assumed profile shapes will probably be satisfactory because the Doppler broadening due to rotation is much more important for line shape than the assumed chemical abundance. We found only one extreme case (NGC 6193 #17 = CD$-$48°11051) for which the He I line strengths were so strong that none of the solar abundance models made a satisfactory fit.

Finally, we note that our assumption about the spin axis orientation angle has a negligible impact on our results. We calculated the line profiles assuming a fixed inclination angle of $i = 90°$, but the actual spin axes of the stars point randomly in space. In order to

determine the consequences of this simplification for the final results, we tested our fitting code using rotationally broadened line profiles made assuming different inclination angles. We found that the line profiles change very little from $i = 90°$ to $i = 30°$ for a fixed geometric value of $V \sin i$, and for the infrequent cases of smaller inclination angle ($i < 30°$) the fitting code can still find the correct $V \sin i$ using a slightly different spectral type.

4. Results and Discussion

We obtained $V \sin i$ measurements for a total of 496 stars in 19 young clusters. Our results for the individual stars in each cluster are listed in Table 3, which is given in full only in the on-line edition. The columns list: (1) the cluster name; (2) WEBDA identification number of the star (coordinates are given in the last column for stars with no WEBDA identification); (3) derived $V \sin i$ averaged over the values obtained from He I $\lambda\lambda 4026, 4387, 4471$, and/or Mg II $\lambda 4481$; (4) the measurement error of $V \sin i$ based on the fit of He I $\lambda 4471$ and/or Mg II $\lambda 4481$; (5), (6), (7) the radial velocity for each observing night, based on measurements of the positions of the He I lines (note that the targets were observed on three nights for NGC 2244 and IC 2944, only one night for Trumpler 14 and 16, and on 2 nights for the rest); (8) the assigned index for spectral subtype of the star (Table 2); and (9) notes for interesting stars, such as double-lined spectroscopic binaries (SB2) or stars having unusual line profiles, where the $V \sin i$ measurement may not be reliable. For double-lined spectroscopic binary systems, the $V \sin i$ values are determined by fitting the dominant component in the double-peaked line profiles. The digital version of Table 3 also gives the mid-exposure heliocentric Julian dates of each observation. There are several instances where we have added some nearby B-type stars to the cluster roster (especially in the case of NGC 2384), and although the cluster membership of these stars needs confirmation, we will assume in the following that all the stars in Table 3 are cluster members.

The radial velocities were obtained by measuring the shift required to match the model and observed profiles and then applying a correction for Earth's motion in the direction of the star. The measurement errors depend on the S/N of the individual spectrum but are typically ± 10 km s^{-1}. However, there are systematic radial velocity errors present in several clusters that are at least this large and that are manifested in overall differences in cluster mean velocity between nights. Our main interest in the velocity data is to identify the radial velocity variable stars that are candidate short period spectroscopic binaries. We adopted a limit of a radial velocity shift greater than 30 km s^{-1} between two nights as the criterion for detection of possible binaries. However, to avoid any systematic shifts in radial velocity between nights, we did not directly use the raw measurements of radial velocity

listed in Table 3 to estimate such variations. Instead, we calculated the mean radial velocity for each night and for every cluster first, and then we compared the residuals (the radial velocity minus the mean) between different nights to find the binaries using the 30 km s^{-1} criterion. This step was done in an iterative way for each cluster: once we found the binary candidates, we removed them from the list and recalculated the mean using the rest of stars and we repeated this isolation of the binary candidates and calculation of the mean until no more stars met the binary star criterion. The velocity variable stars are identified in Table 3 by the notation SB1 in the final column. The stars that we found to be double-lined spectroscopic binaries were also usually velocity variable and these are noted as SB2 in Table 3.

We summarize in Table 4 the results for each of the 19 clusters, which are listed in order of increasing age. The columns here indicate: (1) the common name for the cluster; (2) the logarithm of the cluster age from Loktin, Gerasimenko, & Malysheva (2000); (3) the number N of stars measured; (4) the mean projected rotational velocity of the whole sample; (5) the number n of stars with a pseudo-spectral subtype of B3 or earlier; (6) the mean projected rotational velocity of the subsample of those stars of type B3 or earlier; (7) the number n of very rapid rotators, i.e., stars with a projected rotational velocity greater than 300 km s^{-1}; (8) the number n of candidate spectroscopic binary stars; and (9) the observatory where the spectra were obtained (see Table 1). Note that no binary estimates appear for Trumpler 14 and 16 since we have only single observations available for these clusters. The age determinations from Loktin et al. (2000) are based on fits of cluster color–magnitude diagrams made using isochrones from Bertelli et al. (1994), and although newer and more accurate estimates exist in some cases, we adopt these age determinations here because they form a homogeneous set that should provide a consistent assignment of ages to the clusters in our sample. These age estimates have typical errors of ± 0.2 dex (see Fig. 5 of Loktin et al. 2000).

We begin our review of these results by considering the properties of all the stars in the full sample of clusters. The stars of our sample correspond mainly to MK spectral types from O9.5 to B8.5, and to luminosity classes from III to V. We plot in Figure 3 the mean $V \sin i$ versus pseudo-spectral subtype with the total number of stars in each subtype bin given below. These numbers show that our sample is biased toward earlier subtypes (luminosity biased). The distribution of $V \sin i$ for cluster stars is basically flat over this range and appears to similar the classical diagram for nearby B-type stars presented by Slettebak (1970). There is a slight indication that there are more fast rotators among the late-B subtypes (B5 - B8), which is similar to what Brown & Verschueren (1997) found for stars in Sco OB2 and to what Abt, Levato, & Grosso (2002) found for nearby field stars. However, the differences between the subtype groups are modest. We plot in Figure 4 the

cumulative distribution functions of $V \sin i$ for three subgroups, [O9.5, B1.5], (B1.5, B5.0], and (B5.0, B9.0]. The three curves are all similar to each other and their mean $V \sin i$ values are almost same: 139 km s^{-1}, 154 km s^{-1}, and 151 km s^{-1} for these three groups, respectively.

We next compare the projected rotational velocity distributions of cluster and field B-stars. A histogram of the distribution of $V \sin i$ for all the measured stars (subtypes O9.5 to B8.5) is plotted in Figure 5 (*solid line*). We extracted a subset of similar data for field stars from Abt et al. (2002) for stars with subtypes of B8.5 or earlier and luminosity classes between III and V (737 stars), and we plot the field star histogram also in Figure 5 (*dashed line*). The comparison shows that there are more slow rotators among the field B stars than is the case for the cluster stars. The mean projected rotational velocities are 113 ± 3 km s^{-1} and 148 ± 4 km s^{-1} for the field and cluster stars, respectively (where the quoted errors are the standard deviation of the mean). Part of this difference may be due to the better spectral resolution of the spectra used by Abt et al. (2002) (better able to discern the sharpest-lined stars) and due to the presence of unrecognized binaries in our sample (with blended and broadened line profiles). It is also possible that some real physical causes are responsible for the difference. For example, Strom, Wolff, & Dror (2005) argue that stars formed in denser environments (clusters) appear to rotate faster than field stars. It is also possible that the field stars may represent a somewhat older population (stars from dispersed clusters) so that the difference reflects evolutionary spin-down (see below).

The cumulative distribution function of $V \sin i$ for whole sample is plotted in Figure 6 (*top panel*). We made a 4th order polynomial fit to the cumulative distribution function (shown as a *dotted line* in the *top panel*), and we then obtained an estimate of the $V \sin i$ probability distribution from the derivative of the fit curve (shown as the *dotted line* in *bottom panel*). We next calculated the underlying probability distribution for the stellar equatorial velocity V_{eq} (*dashed line* in the *bottom panel*) from the $V \sin i$ distribution using the deconvolution algorithm from Lucy (1974). The $V \sin i$ distribution of our sample peaks near 100 km s^{-1} while the V_{eq} distribution peaks near 200 km s^{-1}.

We expect that the rotational velocity distributions of single and close binary stars may differ, since binary systems may experience either spin-down through tidal braking or a spin-up from mass transfer. There is evidence of rotational and orbital synchronization among binaries in the field population (Wolff, Edwards, & Preston 1982; Abt et al. 2002). There are 94 variable radial velocity stars (21%) among the 454 stars in our sample with more than one radial velocity measurement that meet the spectroscopic binary criterion we adopted ($\Delta V_r > 30$ km s^{-1}). The mean $V \sin i$ of the candidate binary group is 165 ± 9 km s^{-1} compared to a mean of 144 ± 5 km s^{-1} for the remaining radial velocity constant stars.

This is a somewhat surprising result since synchronously rotating binary stars among the field population have a lower mean $V \sin i$ than single stars (Abt et al. 2002). We wondered if the larger radial velocity measurement errors associated with the rapid rotators (which have broad and shallow lines) led to the accidental inclusion of some rapid rotators in the candidate binary group. Consequently, we selected a second group of binary candidates using a more stringent radial velocity variation criterion ($\Delta V_r > 50$ km s^{-1}). The adoption of this criterion reduces the number of candidate binaries to 49, and the mean $V \sin i$ for this group is even higher, 173 ± 15 km s^{-1}. The cumulative distribution functions for all three groups of stars (single stars, binary stars from the 30 km s^{-1} criterion, and binary stars from the 50 km s^{-1} criterion) are plotted in Figure 7. The Kolmogorov-Smirnov test (KS, hereafter) indicates that there is only a 1% probability that the the single and binary star ($\Delta V_r > 30$ km s^{-1}) data are drawn from the same distribution (or a 3% probability for the binary group selected using the tighter constraint, $\Delta V_r > 50$ km s^{-1}). Thus, the difference appears to be significant. One possible explanation could be that our binary group includes many cases in which a faint or only partially resolved spectral line from the companion causes the composite profile to appear broader and leads to a higher value of $V \sin i$ for such binaries. On the other hand, some of these systems may have experienced a spin-up of the mass gainer due to mass transfer. Follow up spectroscopic investigations of the candidate binaries will be required to determine the precise nature of their projected rotational velocities.

We next turn to the question of temporal changes in the rotational velocity distributions by considering the cluster ages. One way to show the possible evolutionary effects of rotation for B-stars in these clusters is by plotting the $V \sin i$ cumulative distribution functions for clusters of different ages. Since the effects of rotation are expected to occur on time scales comparable to the main sequence lifetime (Heger & Langer 2000; Meynet & Maeder 2000) and since our sample stars (O9 - B9) have dramatically different MS durations, we decided to divide our sample into two groups, high mass ($\geq 9 M_\odot$) and low mass ($< 9 M_\odot$). The main sequence lifetime of a $9 M_\odot$ star is $\log \mathrm{age} = 7.4$ (Schaller et al. 1992), and since most of the clusters we observed are younger than this, only stars in the high mass group in our sample are expected to display evolutionary changes. For each cluster, we first derived the absolute magnitude M_V of a $9 M_\odot$ star at the cluster age using theoretical photometry data from Lejeune & Schaerer (2001). We next transformed this into an apparent magnitude m_V using the reddening-corrected distance modulus of the cluster. Then we assumed that all cluster stars with a magnitude $\leq m_V$ belong to the high mass group, while the fainter stars belong to the low mass group. Ideally, we would like to have a sufficient number of stars of each group in every cluster for statistical analysis, but since we observed fewer than 20 stars in about half of the clusters, this kind of division is impractical. Thus, we grouped clusters with similar ages together into three age bins which have adequate numbers of stars for the

cumulative function plots. The cumulative distribution functions of $V \sin i$ for the different age bins in both high and low mass groups are shown in Figure 8, arranged in panels of 2 columns for the mass groups by 3 rows for the various age bins. Every panel shows two distributions, the cumulative function for all the stars in the corresponding mass group (*filled dots*), which appears the same in each panel of a given column, and the cumulative function for the specific age bin in this mass group (*diamonds*). We also list in each panel the KS probability that the all-age and specific-age binned $V \sin i$ data are drawn from the same distribution.

The expected spin-down is not immediately evident in Figure 8, and, in fact, both mass groups show evidence of a possible spin-up between the first two age bins (perhaps followed by a spin-down in the last age bin). The mean $V \sin i$ values for the three age bins of the high mass group, from young to old, are 119 ± 11, 136 ± 8, and 126 ± 19 km s^{-1} (based upon 67, 111, and 22 stars, respectively). The KS probabilities that the functions are drawn from the same population are 0.28 between the functions shown in the top and middle panels and 0.85 between the functions shown in the middle and bottom panels, respectively. The mean $V \sin i$ values of the three age bins for the low mass group, from young to old, are 156 ± 7, 174 ± 12, and 152 ± 12 km s^{-1} (from samples of 146, 73, and 62 stars, respectively). The KS probabilities are 0.20 between the functions in the top and middle panels and 0.11 between the functions in the middle and bottom panels, respectively. Both groups show that more rapid rotators exist in the middle age bin, which contains clusters somewhat older than 10 Myr.

We plot the mean $V \sin i$ of each cluster against the cluster age in Figures 9 (high mass group) and 10 (low mass group), where we omit those clusters with fewer than 6 measurements. We also plot in Figure 9 (high mass group) theoretical evolutionary tracks of the mean $V \sin i$ for single stars with masses of 9 and $12 M_\odot$ based on the results from Meynet & Maeder (2000). We assumed that all clusters begin with a distribution of stellar rotational velocities given by the $V_{\rm eq}$ distribution in Figure 6. Then we used the Meynet & Maeder (2000) model results to calculate how each $V_{\rm eq}$ point is transformed to a lower velocity at each time step in order to determine a new mean $V_{\rm eq}$ for that time step. The physical mean $< V_{\rm eq} >$ was then transformed into the projected mean $< V \sin i >$ by multiplying a factor of $\pi/4$ (assuming that the spin axes of stars point randomly in space). With a few exceptions, most of the cluster means in Figure 9 appear to fall within the region defined by the theoretically predicted spin down tracks. However, both Figures 9 and 10 confirm the impression from Figure 8 that clusters in the age range $7.0 < \log {\rm age} < 7.15$ seem to contain more rapid rotators.

We expect that rapid rotators originate in three ways: 1) stars that are born as very

rapid rotators and maintain their spin throughout the MS phase; 2) mass transfer in a binary system can turn the mass gainer into a very rapid rotator; and 3) the core contraction of a star at the TAMS can cause a spin-up. The last possibility can be investigated by considering the the locations of the rapid rotators in the cluster HRD. We selected four clusters that each contain a significant number of rapidly rotating stars with $V \sin i > 260$ km s^{-1}. The two clusters with the fastest mean $V \sin i$ are NGC 3293 and Berkeley 86, and both of these have an age near 10 Myr. We found that 9 of the 23 stars we observed in NGC 3293 have $V \sin i > 260$ km s^{-1} (and one additional fast rotator was identified by Balona 1975b). There are 4 of 17 stars with $V \sin i > 260$ km s^{-1} among those observed in the cluster Berkeley 86. We also considered two older clusters, NGC 4755 and NGC 457, for which we identified 5 of 33 stars and 3 of 19 stars, respectively, with $V \sin i > 260$ km s^{-1}. We plot the positions of all these fast rotators in color-magnitude diagrams in Figure 11. Only two of these stars are found near the TAMS in the region where single star models predict that the spin-up may occur (NGC 3293 #19 and Berkeley 86 #9). We caution that even the positions of these two stars may be artificially shifted to redder colors by rotation and gravity darkening and so they may not actually be TAMS objects. The rapid rotators appear to be located throughout the band from the ZAMS to the TAMS in the HRD much as are the rapidly rotating Be stars (Zorec 2004; McSwain & Gies 2005). This suggests that the fast rotators observed in these clusters are not generally the result of the predicted core adjustment that occurs at TAMS.

However, clusters with an age of ≈ 10 Myr probably contain close binary systems that are old enough for the evolutionary expansion and Roche lobe overflow to occur, and the mass gainers could be spun up to become rapid rotators (see the study of the Algol binary RY Per by Barai et al. 2004). We find evidence for only two candidate binaries among these rapid rotators (NGC 3293 #83 = CPD$-57°3501$, and NGC 457 #43), but post-mass transfer binaries are probably not easily detected in our survey since they probably have long orbital periods and small radial velocity semi-amplitudes (see, for example, the study of the Be binary ϕ Per by Gies et al. 1998). Models of the binary spin-up process (Pols et al. 1991; Van Bever & Vanbeveren 1997) suggest that most of the mass gainer stars will appear among the more massive stars near the top of the main sequence. It will be important to compare our results on the rotational velocities of the brighter cluster members with investigations of the rotational properties of the fainter, lower mass population in order to test this prediction.

Our approach in this paper was to group individual stars according to cluster membership and age to study how the rotational velocity distribution varies with time. However, since the predicted evolutionary time scales vary with stellar mass, we are probably losing some information on the rotational evolution by averaging over samples with a significant range in stellar mass. In the next paper in this series (Huang & Gies 2006), we will present a

scheme we have developed to determine the effective temperature, gravity, and helium abundance for each of our targets, and we will present additional evidence for the evolutionary spin down that is predicted to occur for massive rotating stars.

REFERENCES

Abt, H. A, Levato, H., & Grosso, M. 2002, ApJ, 573, 359

Ardeberg, A., & Maurice, E. 1977, A&AS, 28, 153

Arnal, M., Morrell, N., Garcia, B., & Levato, H. 1988, PASP, 100, 1076

Arp, H. C., & van Sant, C. T. 1958, AJ, 63, 341

Balona, L. A. 1975a, Mem. Roy. Astron. Soc., 78, 51

Balona, L. A. 1975b, MNRAS, 173, 449

Barai, P., et al. 2004, ApJ, 608, 989

Barden, S. C., & Armandroff, T. 1995, in Fiber Optics in Astronomical Applications, ed. S. C. Barden, SPIE Vol. 2476, 56

Bertelli, G., Bressan, A., Chiosi, C., Fagotto, F., & Nasi, E. 1994, A&AS, 106, 275

Boden, E. 1946, Uppsala Astr. Obs. Ann., 2, 1

Brown, A. G. A., & Verschueren, W. 1997, A&A, 319, 811

Clariá, J. J., Lapasset, E., Piatti, A. E., & Ahumada, A. V. 2003, A&A, 409, 541

Collins, G. W., II, & Harrington, J. P. 1966, ApJ, 146, 152

Dachs, J., & Kaiser, D. 1984, A&AS, 58, 411

Dworetsky, M. M. 1975, AJ, 80, 131

Etzel, P. B., & Olson, E. C. 1993, AJ, 106, 1200

Fabregat, J., & Torrejón, J. M. 2000, A&A, 357, 451

Feinstein, A., Marraco, H. G., & Muzzio, J. C. 1973, A&AS, 12, 331

Forbes, D. 1981, PASP, 93, 441

Forbes, D., English, D., & de Robertis, M. M. 1992, AJ, 103, 916

Gies, D. R., Bagnuolo, W. G., Jr., Ferrara, E. C., Kaye, A. B., Thaller, M. L., Penny, L. R., & Peters, G. J. 1998, ApJ, 493, 440

Gray, D. F. 1992, The Observation and Analysis of Stellar Atmospheres, 2nd edition (Cambridge: Cambridge Univ. Press)

Hanson, M. M., Howarth, I. D., & Conti, P. S. 1997, ApJ, 489, 698

Heger, A., & Langer, N. 2000, ApJ, 544, 1016

Hill, G. 1967, ApJS, 14, 263

Hoag, A. A., Johnson, H. L., Iriarte, B., Mitchell, R. I., Hallam, K. L., & Sharpless, S. 1961, Publ. U.S. Naval Obs. Second Series, 17, 345

Howarth, I. D., Siebert, K. W., Hussain, G. A. J., & Prinja, R. K. 1997, MNRAS, 284, 265

Howarth, I. D., & Smith, K. C. 2001, MNRAS, 327, 353

Huang, W., & Gies, D. R. 2006, ApJ, submitted (astro-ph/0510720)

Hubeny, I., & Lanz, T. 1995, ApJ, 439, 875

Johnson, H. L. 1950, ApJ, 112, 240

Langer, N., Yoon, S.-C., Petrovic, J., & Heger, A. 2004, in Stellar Rotation, Proc. IAU Symp. 215, ed. A. Maeder & P. Eenens (San Francisco: ASP), 535

Lejeune, T., & Schaerer, D. 2001, A&A, 366, 538

Lodén, L. O. 1966, Arkiv för Astronomii, 4, 65

Loktin, A.V., Gerasimenko, T.P., & Malysheva, L.K. 2001, Astron. Astrophys. Trans., 20, 607

Lucy, L. B. 1974, AJ, 79, 745

Maeder, A., Grebel, E. K., & Mermilliod, J.-C. 1999, A&A, 346, 459

Massey, P., Johnson, K. E., & DeGioia-Eastwood, K. 1995, ApJ, 454, 151

Mathys, G. 2004, in Stellar Rotation, Proc. IAU Symp. 215, ed. A. Maeder & P. Eenens (San Francisco: ASP), 270

Mathys, G., Andrievsky, S. M., Barbuy, B., Cunha, K., & Korotin, S.A. 2002, A&A, 387, 890

McSwain, M. V., & Gies, D. R. 2005, ApJS, 161, 118

Mermilliod, J.-C. 1982, A&A, 109, 48

Mermilliod, J.-C., & Paunzen, E. 2003, A&A, 410, 511

Meynet, G., & Maeder, A. 1997, A&A, 321, 465

Meynet, G., & Maeder, A. 2000, A&A, 361, 101

Moffat, A. F. J., & Vogt, N. 1973, A&AS, 10, 135

Ogura, K., & Ishida, K. 1981, PASJ, 33, 149

Oosterhoff, P. T. 1937, Ann. Sternw. Leiden, 17, 1

Penny, L. R. 1996, ApJ, 463, 747

Perry, C. L., Franklin, C. B., Landolt, A. U., & Crawford, D. L. 1976, AJ, 81, 632

Pesch, P. 1959, ApJ, 130, 764

Pols, O. R., Coté, J., Waters, L. B. F. M., & Heise, J. 1991, A&A, 241, 419

Purgathofer, A. 1964, Ann. Univ. Sternw. Wien, 26, 37

Schaller, G., Schaerer, D., Meynet, G., & Maeder, A. 1992, A&AS, 96, 269

Šimon, V. 1999, A&AS, 134, 1

Slettebak, A. 1965, ApJ, 145, 121

Slettebak, A. 1968, ApJ, 154, 933

Slettebak, A. 1970, in Stellar Rotation, Proc. IAU Coll. 4, ed. A. Slettebak (Dordrecht: Reidel), 3

Slettebak, A. 1985, ApJS, 59, 769

Slettebak, A., Collins, G. W., II, Parkinson, T. D., Boyce, P. B., & White, N. M. 1975, ApJS, 29, 137

Strom, S. E., Wolff, S. C., & Dror, D. H. A. 2005, AJ, 129, 809

Townsend, R. H. D., Owocki, S. P., & Howarth, I. D. 2004, MNRAS, 350, 189

Turner, D. G., Grieve, G. R., Herbst, W., & Harris, W. E. 1980, AJ, 85, 1193

Valdes, F. 1992, Guide to the HYDRA Reduction Task DOHYDRA (Tucson: NOAO)

Van Bever, J., & Vanbeveren, D. 1997, A&A, 322, 116

van den Heuvel, E. P. J. 1970, in Stellar Rotation, ed. A. Slettebak (Dordrecht: Reidel), 178

van Schewick, H. 1966, Veroeff. Univ. Sternw. Bonn, 74, 1

Vasilevskis, S., Sanders, W. L., & van Altena, W. F. 1965, AJ, 70, 806

Verschueren, W. 1991, Thesis (Free Univ. Brussels)

Vogt, N., & Moffat A. F. J. 1972, A&AS, 7, 133

Wolff, S. C. 1981, ApJ, 244, 221

Wolff, S. C., Edwards, S., & Preston, G. W., 1982, ApJ, 252, 322

Zorec, J. 2004, in Stellar Rotation, Proc. IAU Symp. 215, ed. A. Maeder & P. Eenens (San Francisco: ASP), 73

Table 1.   Hydra Observing Runs

Parameter	WIYN 3.5 m	CTIO 4.0 m
UT Dates	2000 Nov. 13 – 16	2001 Feb. 9 – 12
Fiber diameter (μm)	310	300
Camera name	Simmons	Bench Schmidt
Camera focal length (mm)	381	400
Grating name	1200@28.7	KPGLD
Grating grooves mm^{-1}	1200	790
Grating blaze angle (deg)	28.7	19.6
Order	2	2
Order sorting filter	CuSO4	BG-39
CCD detector	SITe 2×2K	SITe 2×4K
CCD pixel size (μm)	24	15
Reciprocal dispersion (Å pixel^{-1})	0.252	0.440
Wavelength range (Å)	3983 – 4501	3878 – 4781
Comparison source	CuAr	He-Ne-Ar
FWHM at 4026 Å (Å)	0.74	1.74
FWHM at 4387 Å (Å)	0.83	1.44
FWHM at 4471 Å (Å)	0.85	1.42

Table 2.   ZAMS Model Star Parameters

Index	Pseudo-Spectral Subtype	T_{eff} (kK)	M ($M_{\odot}$)	R ($R_{\odot}$)
0....	O9.5 V	34.9	20.0	5.8
1....	O9.8 V	32.6	17.0	5.3
2....	B0.0 V	31.1	15.0	5.0
3....	B0.3 V	29.1	12.6	4.6
4....	B0.5 V	27.8	11.0	4.3
5....	B1.0 V	25.5	9.5	4.0
6....	B1.5 V	23.7	8.3	3.7
7....	B2.0 V	22.0	7.0	3.3
8....	B2.5 V	20.3	6.3	3.1
9....	B3.0 V	18.7	5.5	2.9
10....	B3.5 V	17.8	5.1	2.9
11....	B4.0 V	17.0	4.8	2.8
12....	B4.5 V	16.2	4.4	2.8
13....	B5.0 V	15.4	4.0	2.7
14....	B5.5 V	14.9	3.8	2.6
15....	B6.0 V	14.4	3.6	2.5
16....	B6.5 V	13.9	3.4	2.5
17....	B7.0 V	13.5	3.3	2.4
18....	B7.5 V	13.0	3.2	2.3
19....	B8.0 V	12.6	2.9	2.2
20....	B8.5 V	11.8	1.8	2.1

Table 3.   Projected Rotational Velocities of B Stars in 19 Open Clusters[a]

Cluster Name	WEBDA Number	$V \sin i$ (km s^{-1})	$\delta V \sin i$ (km s^{-1})	$V_r(N1)$ (km s^{-1})	$V_r(N2)$ (km s^{-1})	$V_r(N3)$ (km s^{-1})	Pseudo-Spectral Subtype Index	Notes
Ber 86 .	1	184	7	30.3	30.8	$\cdots$	1.3	$\cdots$
Ber 86 .	3	192	10	-24.6	7.5	$\cdots$	4.0	SB2
Ber 86 .	4	178	8	17.2	45.2	$\cdots$	1.0	SB2
Ber 86 .	9	362	21	-7.6	-15.7	$\cdots$	3.3	$\cdots$

[a]The full version of this table appears in the on-line edition.

Table 4.   Summary Data for 19 Open Clusters

Name	log age (yr)	N	$< V \sin i >$ (All) (km s^{-1})	n ($\leq$ B3)	$< V \sin i >$ ($\leq$ B3) (km s^{-1})	n ($V \sin i >$ 300 km s^{-1})[a]	n (Binary)[a]	Obs.
NGC 6193 .	6.78	20	155	15	134	2 (10)	4 (20)	CTIO
Trumpler 16	6.79	35	135	27	150	2 (6)	$\cdots$	CTIO
IC 1805 ...	6.82	30	145	25	147	1 (3)	9 (30)	WIYN
IC 2944 ...	6.82	38	136	25	127	2 (5)	5 (13)	CTIO
Trumpler 14	6.83	6	109	2	178	0 (0)	$\cdots$	CTIO
NGC 2244 .	6.90	41	168	15	153	5 (12)	16 (39)	WIYN
NGC 2384 .	6.90	15	91	8	83	0 (0)	1 (7)	CTIO
NGC 2362 .	6.91	28	161	11	141	1 (4)	4 (14)	CTIO
NGC 3293 .	7.01	23	184	20	178	5 (22)	2 (9)	CTIO
NGC 884 ..	7.03	57	149	48	140	4 (7)	14 (25)	WIYN
NGC 1502 .	7.05	18	166	12	183	2 (11)	5 (28)	WIYN
NGC 869 ..	7.07	55	121	49	113	2 (4)	14 (25)	WIYN
NGC 2467 .	7.10	14	150	4	167	1 (7)	2 (14)	CTIO
Berkeley 86	7.12	17	194	15	181	3 (18)	1 (6)	WIYN
IC 2395 ...	7.22	16	113	3	94	0 (0)	2 (13)	CTIO
NGC 4755 .	7.22	33	141	18	151	1 (3)	3 (9)	CTIO
NGC 7160 .	7.28	16	183	5	177	2 (13)	4 (25)	WIYN
NGC 457 ..	7.32	19	150	10	173	1 (5)	6 (32)	WIYN
NGC 2422 .	7.86	15	143	1	245	1 (7)	2 (13)	WIYN

[a]The number in parentheses is the percentage.
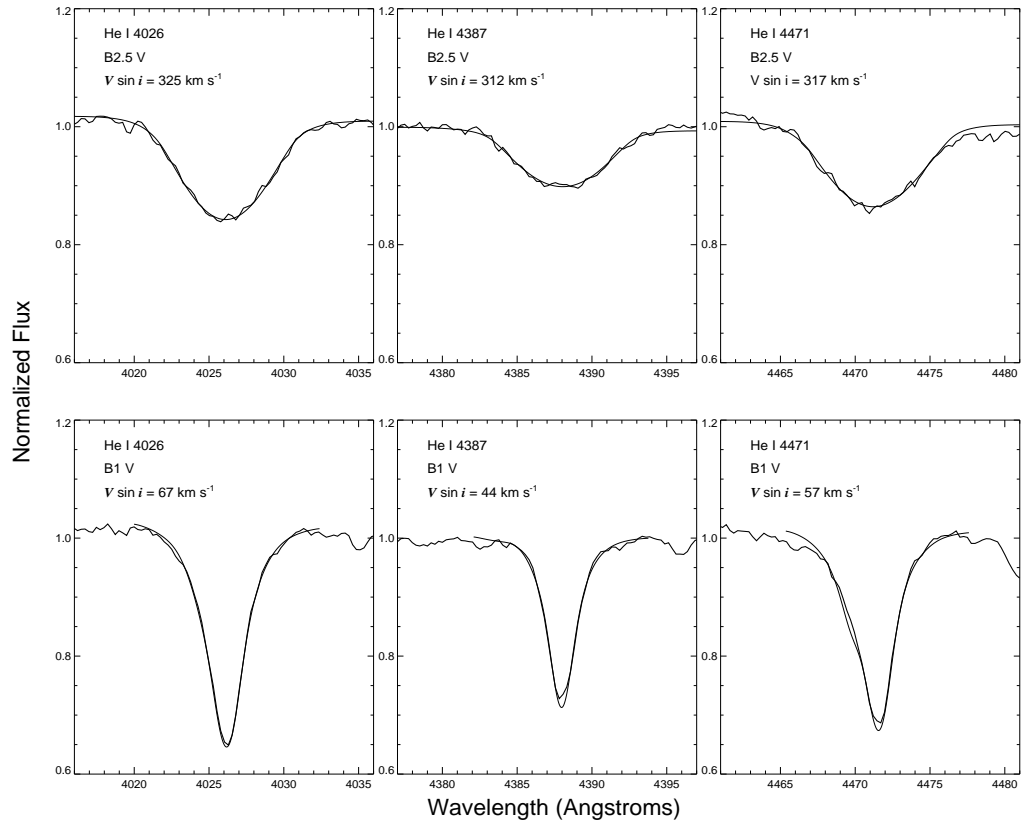
Fig. 1.— Fitting results for the He I lines (*thin lines*) compared with observed profiles (*thick lines*). The top panels show fits for a fast rotator, NGC 884 #2255, while the bottom panel shows the same for a slow rotator, NGC 884 #1983.
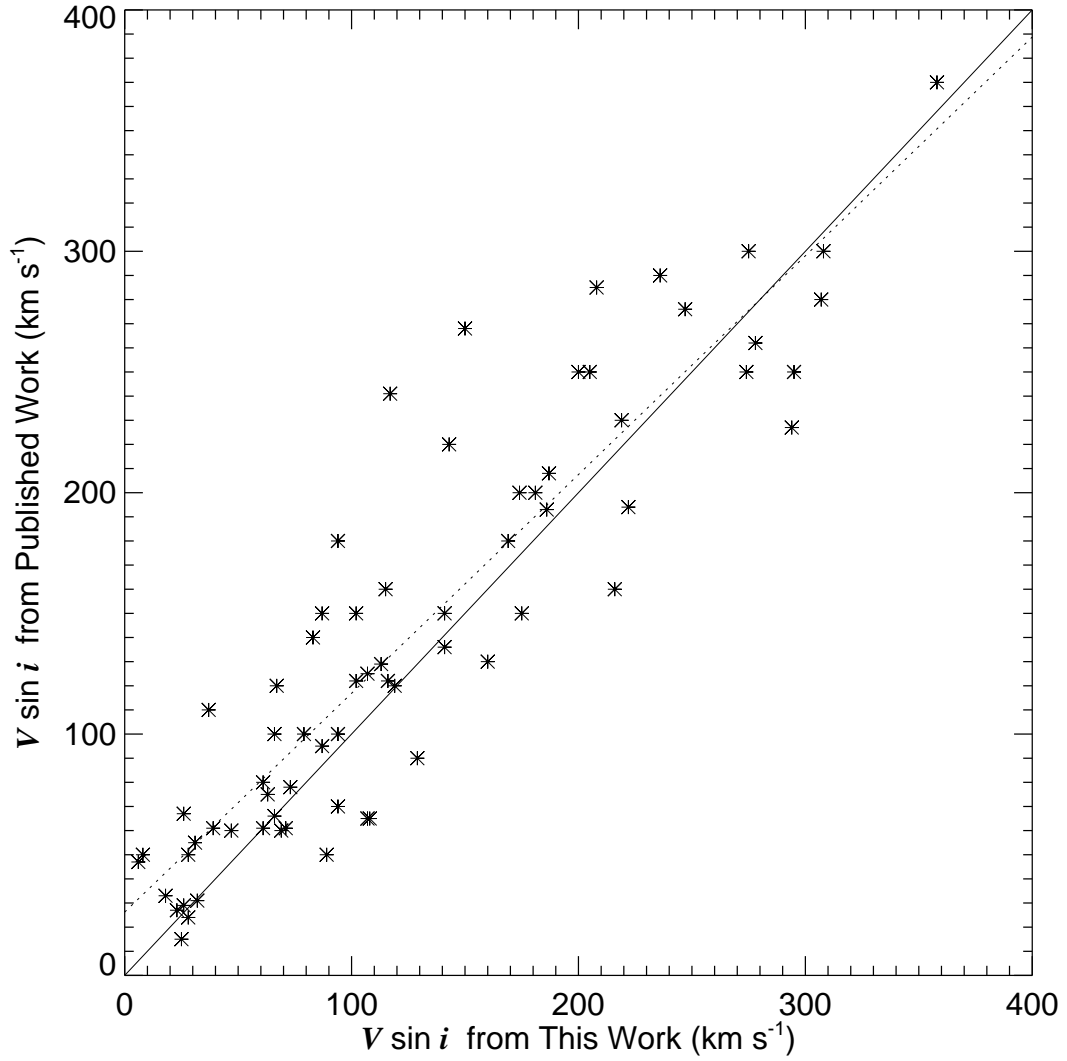
Fig. 2.— A comparison of our measured $V \sin i$ values with published work. The solid line shows the one-to-one relationship while the dotted line is the result of a linear least-squares fit.
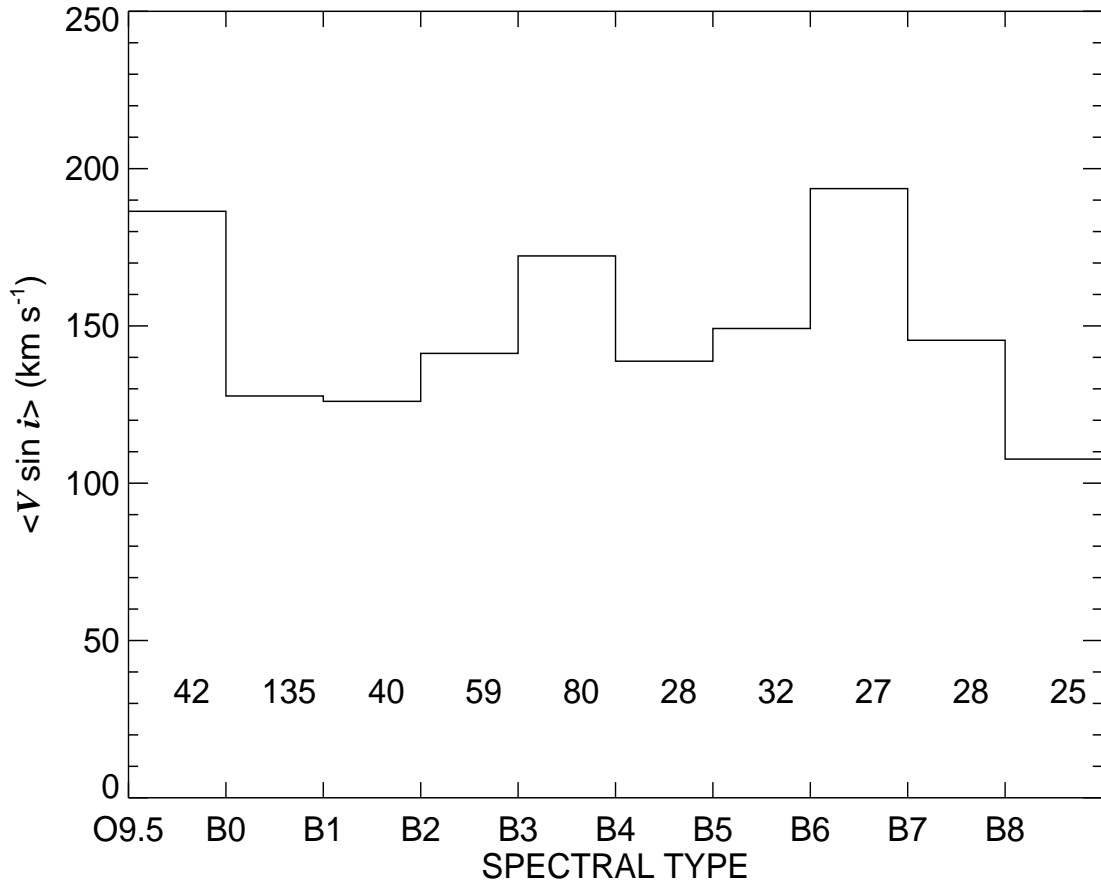
Fig. 3.— Mean $V \sin i$ as a function of pseudo-spectral subtype. The number of stars in each subtype bin is given at the bottom.
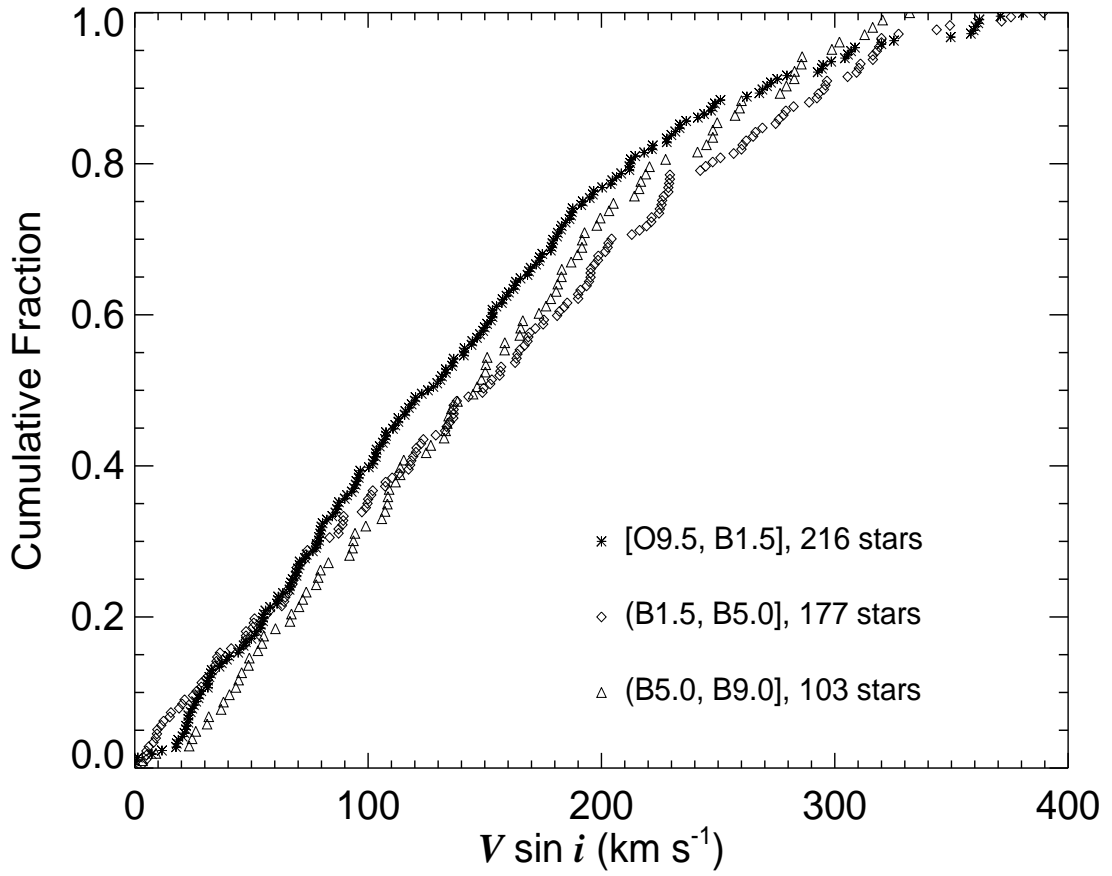
Fig. 4.— The cumulative distribution functions of $V \sin i$ for the stars gathered into three groupings of pseudo-spectral subtype. The subtype range is given using the mathematical notation in which "[" means the boundary is included while "(" means the boundary is not included.
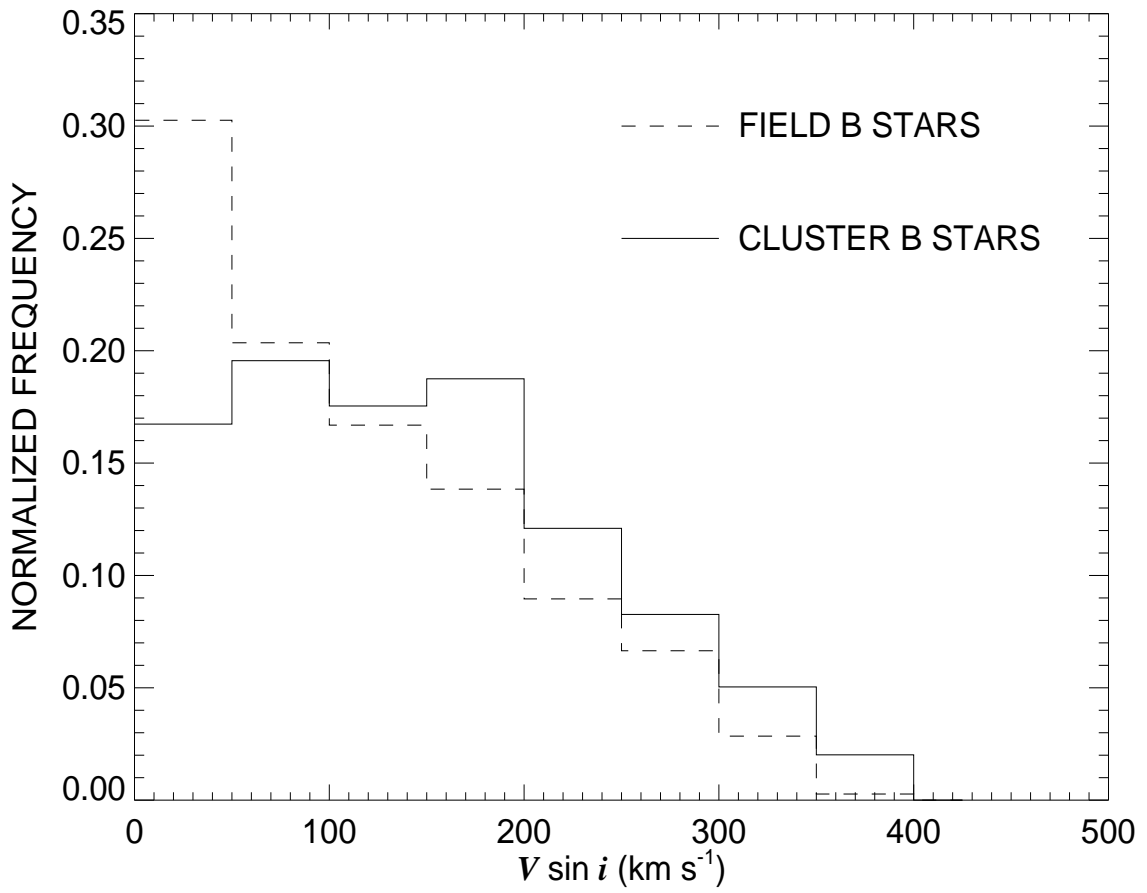
Fig. 5.— Histograms of $V \sin i$ for field stars (Abt et al. 2002) (*dashed line*) and for cluster stars (*solid line*).
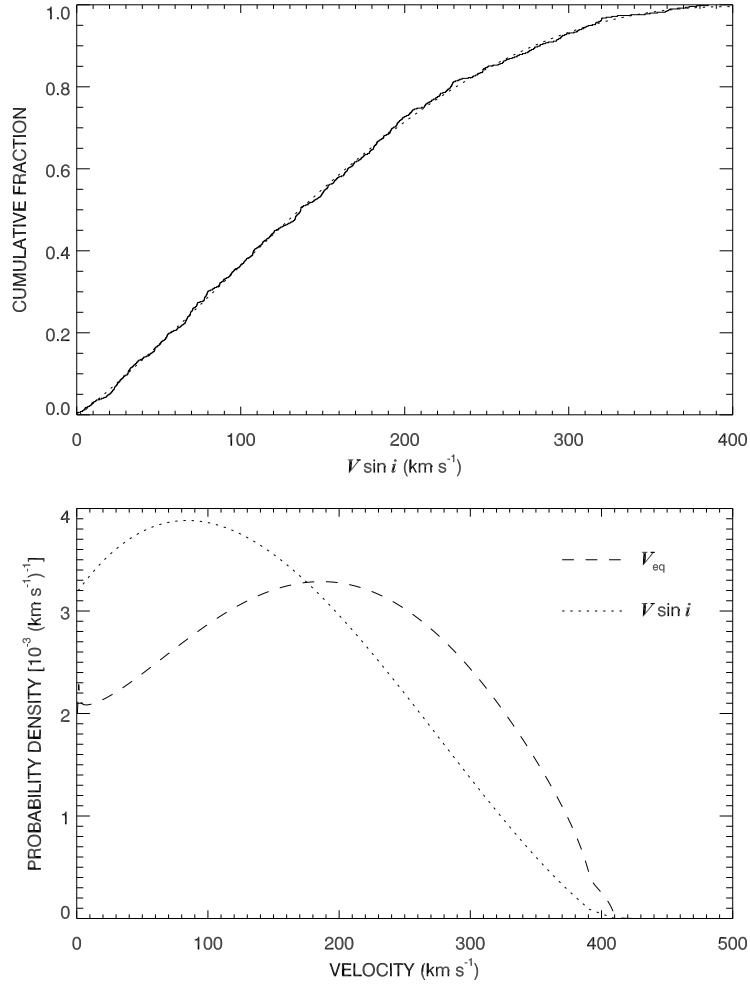
Fig. 6.— *Top panel:* the cumulative distribution function of $V \sin i$ for the entire sample of 496 stars (*solid line*) and its polynomial fit (*dotted line*). *Bottom panel:* the $V \sin i$ distribution derived from the polynomial fit (*dotted line*) and the associated distribution of equatorial velocity V_{eq} (*dashed line*).
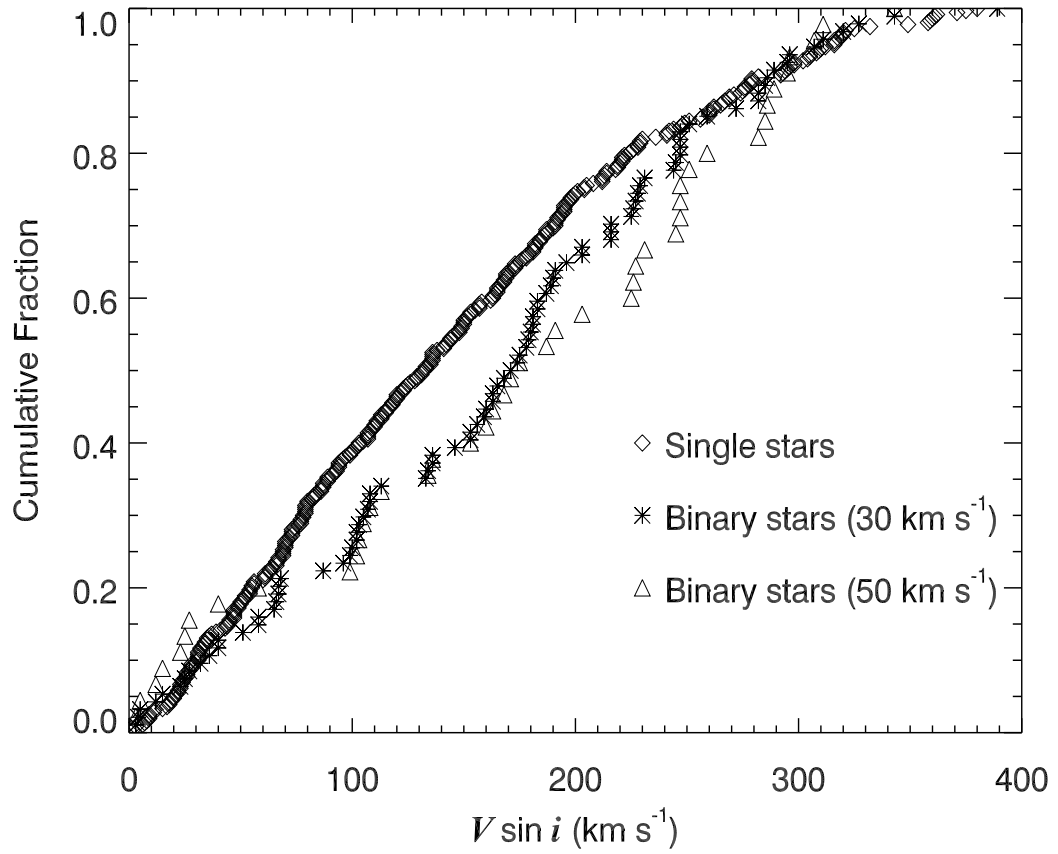
Fig. 7.— The cumulative distribution functions of $V \sin i$ for single and candidate binary stars (according to two criteria for the minimum radial velocity range).
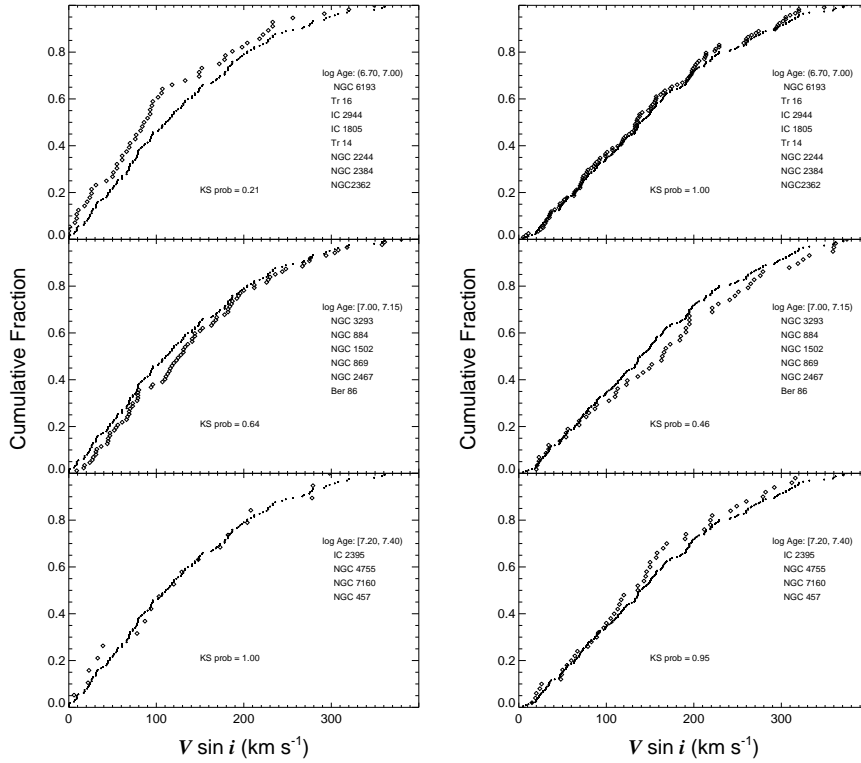
Fig. 8.— The cumulative distribution functions of $V \sin i$ for the subgroups of high mass ($M \geq 9 M_\odot$, *left* column) and low mass ($M < 9 M_\odot$, *right* column) stars at different ages (increasing from top to bottom). Each panel has two curves: one is the function for the specific-age subgroup (*diamonds*) while the other is the function for all the stars of the three panels together (*filled circles*). The KS probability that the two samples are drawn from the same parent distribution is listed in each case.
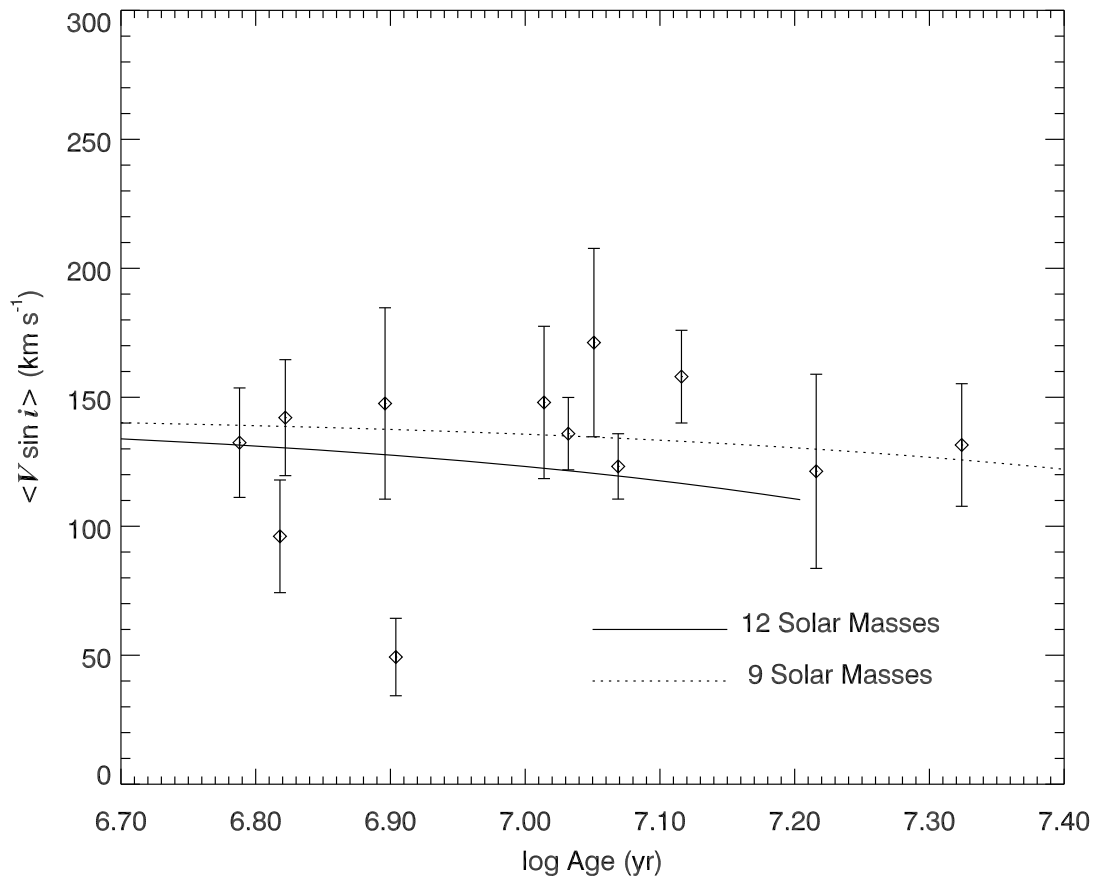
Fig. 9.— Mean $V \sin i$ for high mass stars $(M \geq 9 M_\odot)$ in young clusters plotted against logarithm of cluster age. The solid line and dotted line show the prediction from Meynet & Maeder (2000) for an ensemble of $12 M_\odot$ and $9 M_\odot$ stars, respectively.
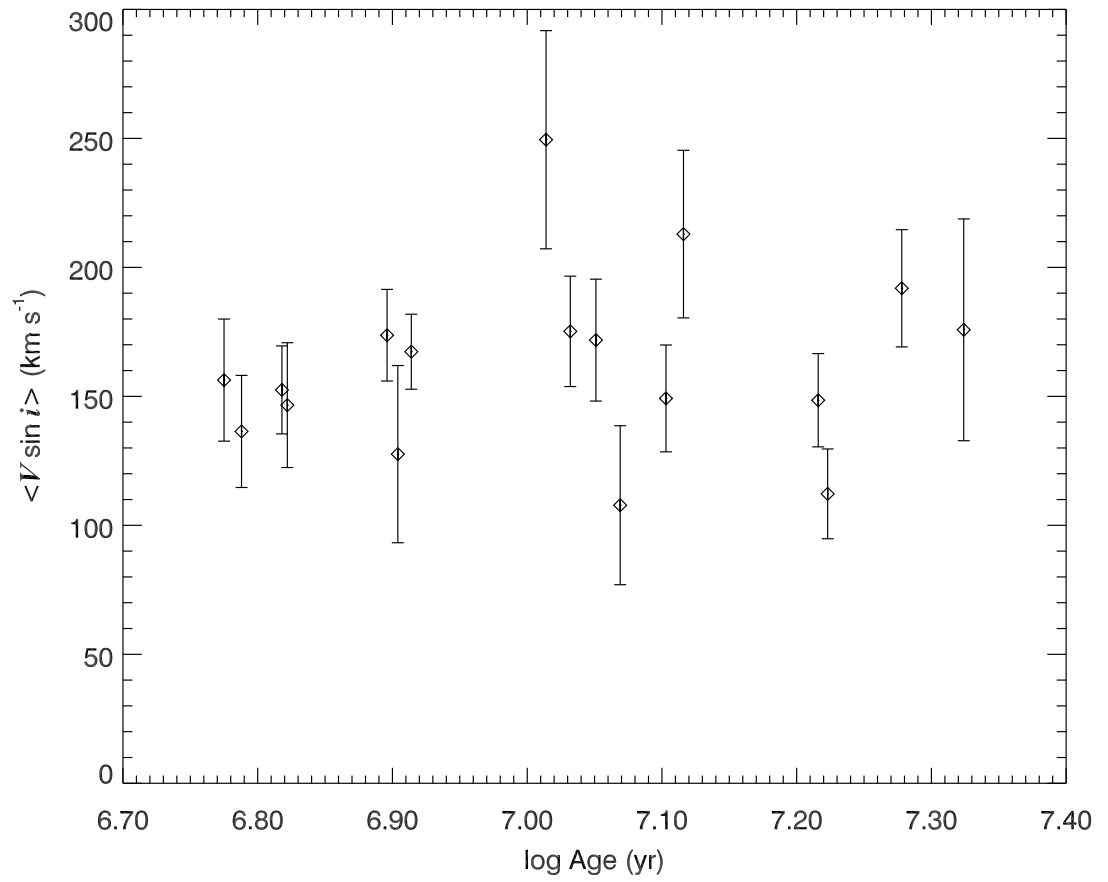
Fig. 10.— Mean $V \sin i$ for stars ($M < 9 M_\odot$) in young clusters plotted against logarithm of cluster age.
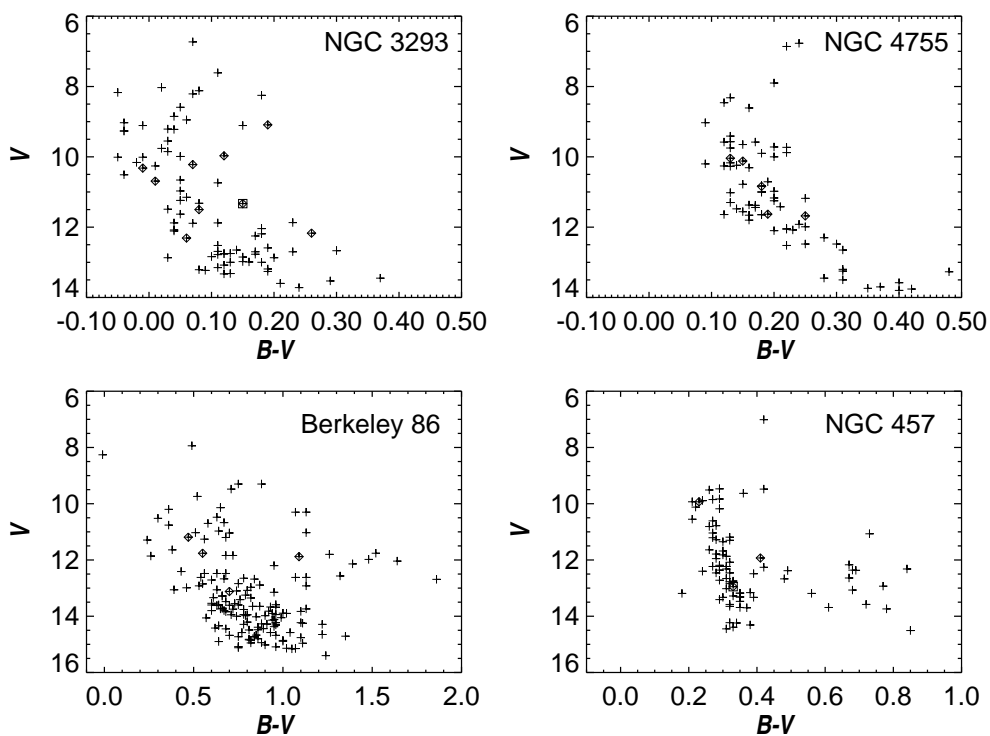
Fig. 11.— Color-magnitude diagrams for NGC 3293 (from photometry by Turner et al. 1980), Berkeley 86 (photometry by Forbes, English, & de Robertis 1992 and Massey, Johnson, & DeGioia-Eastwood 1995), NGC 4755 (photometry by Perry et al. 1976 and Dachs & Kaiser 1984), and NGC 457 (photometry by Pesch 1959 and Hoag et al. 1961). The crosses enclosed in diamonds mark the fast rotators ($V \sin i > 260$ km s^{-1}). The only two candidate binary stars identified among the fast rotators are NGC 3293 #83 and NGC 457 #43, which are marked by enclosing squares.